The hydrogeological information in cross-borehole complex conductivity data from an unconsolidated conglomeratic sedimentary aquifer

Journal:	*Geophysics*
Manuscript ID	GEO-2015-0608.R1
Manuscript Type:	Technical Paper
Date Submitted by the Author:	n/a
Complete List of Authors:	Binley, Andrew; Lancaster University, Lancaster Environment Centre Keery, John; Lancaster University, Lancaster Environment Centre Slater, Lee; Rutgers University-Newark Barrash, Warren; Boise State University, Geosciences; Cardiff, Michael; University of Wisconsin-Madison
Keywords:	groundwater, induced polarization (IP), permeability, electrical/resistivity, 3D
Area of Expertise:	Electrical and Electromagnetic Methods

SCHOLARONE™
Manuscripts

The hydrogeological information in cross-borehole complex conductivity data

from an unconsolidated conglomeratic sedimentary aquifer

Andrew Binley[1], John Keery[1], Lee Slater[2], Warren Barrash[3], Mike Cardiff[4]

Right Running Head: Cross-borehole complex conductivity

1: Lancaster University, Lancaster, UK, E-mail: a.binley@lancaster.ac.uk ,

john@shutterstone.co.uk

2: Rutgers University-Newark, Newark, NJ, USA, E-mail: lslater@rutgers.edu

3: Boise State University, Boise, ID, USA, E-mail: wbarrash@cgiss.boisestate.edu

4: University of Wisconsin-Madison, WI, USA, E-mail: cardiff@wisc.edu

ABSTRACT

18 Accurate estimation of the hydrological properties of near-surface aquifers is important since

19 these properties strongly influence groundwater flow and solute transport. Laboratory-based

20 investigations have indicated that induced polarization (IP) properties of porous media may be

21 linked, through either semi-empirical or fully mechanistic models, to hydrological properties,

22 including hydraulic conductivity. There is, therefore, a need for field assessments of the value of

23 IP measurements in providing insights into the hydrological properties of aquifers. A cross-

24 borehole IP survey was carried out at the Boise Hydrogeophysical Research Site (BHRS), an

25 unconsolidated fluvial aquifer which has previously been well studied with a variety of

26 geophysical and hydrogeological techniques. High quality IP measurements were inverted, with

27 careful consideration of the data error structure, to provide a 3-D distribution of complex

28 electrical conductivity values. The inverted distribution was further simplified using k-means

29 cluster analysis to divide the inverted volume into discrete zones with horizontal layering.

30 Identified layers based on complex electrical conductivity inversions are in broad agreement with

31 stratigraphic units identified in previous studies at the site. Although mostly subtle variations in

32 the phase angle are recovered through inversion of field data, greater contrasts in the IP data are

33 evident at some unit boundaries. However, in coarse grained aquifers, such as the BHRS, the

34 discrimination of mildly contrasting lithologic units and associated changes in hydraulic

35 conductivity of one or two orders of magnitude are unlikely to be achieved through field IP

36 surveys. Despite the difficulty of differentiating subtle differences between all units, overall

37 estimates of hydraulic conductivity purely from our field IP data are typically within an order of

38 magnitude of independently-measured values.

39

40   INTRODUCTION

41

42   Three-dimensional (3-D) high-resolution information on shallow subsurface structure is needed

43   to improve understanding of groundwater flow, vadose zone moisture dynamics and solute

44   transport. Such structural information can improve conceptual models required to develop

45   realistic flow and transport simulations. Geophysical imaging has been extensively employed for

46   this purpose, driven by technological developments that permit faster and less expensive

47   acquisition of 3-D datasets (e.g. Griffiths and Turnbull, 1985; Loke et al., 2013; Stummer et al.,

48   2002). Beyond structural information, it may be possible to estimate hydraulic properties (e.g.,

49   porosity ($\emptyset$), or ultimately hydraulic conductivity (K)) if reliable petrophysical relations can be

50   applied to geophysical images. In particular, the determination of K distributions from

51   geophysical images has been extensively pursued, although experience suggests that achieving

52   this goal requires information from more than a single type of geophysical measurement (e.g.

53   Doetsch et al., 2012; Jardani et al., 2013).

54

55   Electrical methods hold significant promise because of established physical links to

56   hydrogeological parameters (e.g., $\emptyset$, pore size distribution, grain size distribution and surface

57   area) which influence K (e.g. Revil and Florsch, 2010; Slater and Lesmes, 2002b). Furthermore,

58   electrical measurements can be acquired over a wide range of scales and with different methods,

59   electrode types and configurations. The DC resistivity imaging method has been widely applied

60   (e.g. Bentley and Gharibi, 2004; Cassiani et al., 2006; Jardani et al., 2013) but is limited in that

61   quantitative hydrogeological information is challenging to extract from a single type of

62   geophysical measurement, even with generally available basic supporting information such as

63 rock or sediment type (e.g., sand or sand with silt or clay). The complex conductivity (or

64 induced polarization) method holds promise for improving quantification of hydrogeological

65 properties as information on both the interconnected pore volume (e.g. $\emptyset$, tortuosity) and

66 mineral-fluid interfacial area (e.g. surface area to pore volume (S_{por}), effective grain size) can in

67 principle be derived from the complex electrical measurements (Börner et al., 1996; Slater and

68 Lesmes, 2002a; Weller et al., 2013). Recent advances have been made (e.g. Revil and Florsch,

69 2010; Slater and Lesmes, 2002b; Weller et al.,2015) in understanding the link between complex

70 conductivity and hydraulic conductivity – mainly through empirical or semi-empirical models,

71 for example assuming Kozeny-Carman and Archie petrophysics (Archie, 1942; Charbeneau,

72 1999). However, although inversion tools are now well established for field application, few

73 studies have attempted to assess the potential of complex conductivity imaging for deriving

74 hydrogeological information (but see, for example, Hördt et al., 2009; Attwa and Günther, 2013).

75 Furthermore, previous field studies have considered a wide range of hydrologic parameter

76 variation i.e. several orders of magnitude change in K (Hördt et al., 2007; Kemna et al., 2004;

77 Slater and Glaser, 2003), but in some field settings more subtle contrasts in hydrogeophysical

78 properties significantly influence the overall system behavior (Sudicky, 1986).

79

80 Few, if any, field-scale complex conductivity studies have had strong independent datasets on

81 electrical and hydrologic parameters of the system required for evaluating the information

82 obtainable from the complex conductivity inversion. Here, we report on complex conductivity

83 imaging from a local-scale study (15-20 m in all three directions) performed to advance our

84 understanding of the hydrogeological information (qualitative, semi-quantitative and

85 quantitative) that can be obtained from IP. We take advantage of an exceptionally well-studied

86   natural unconsolidated sedimentary aquifer where results from previous borehole and borehole-

87   to-borehole geophysical surveys allow us to assess the performance of the complex conductivity

88   imaging. Where such borehole arrays are available in unconsolidated aquifers, the spatial

89   characterization of hydraulic conductivity can be estimated by slug tests (e.g. Barrash and

90   Cardiff, 2013; Brauchler et al., 2010; Cardiff et al., 2011; Diem et al., 2010), pumping tests (e.g.

91   Barrash et al., 2006; Cardiff et al., 2009), and by 3-D hydraulic tomography (Cardiff et al., 2012;

92   2013).

93

94   The aim of this work is to evaluate the variation in complex electrical conductivity derived from

95   inversion of field data where high resolution characterization of hydrogeological properties

96   already exists. Specifically, we aim to: (1) assess the contrast in complex conductivity that

97   results from the variability in physical properties; (2) determine the link (if any) between

98   complex conductivity variability and known hydrostratigraphy; (3) assess the relative value of

99   DC conductivity versus complex conductivity for independent delineation of lithological units;

100   and (4) offer evidence-based insight into the potential value of field-scale complex conductivity

101   for direct quantitative estimation of key hydrogeophysical properties in similar settings. Slater et

102   al. (2014) describe high accuracy laboratory spectral induced polarization (SIP) measurements

103   on samples extracted from the study site of this work showing differences in the complex

104   conductivity magnitude associated with grain size variations. However, subtle variations in the

105   polarization relaxation time distributions between units could not be correlated with unit physical

106   properties. We therefore restrict our analysis to inversion of the complex conductivity only, and

107   do not consider more elaborate inversion methods recently developed to analyze the spectral

108   characteristics of the polarization response time domain data (e.g., Fiandaca et al.,2013).

5

ELECTRICAL PROPERTIES

Complex electrical conductivity (σ^*) quantifies the ability of a porous medium to transport and store charge. It is usually determined from measurements of the conductivity magnitude ($|\sigma|$) and phase shift (φ) of a porous material relative to a reference resistor. The real (σ') and imaginary (σ'') components of σ^* represent electromigration (transport of charge under the influence of an electric field) and polarization (reversible storage of charge under the influence of an electric field) mechanisms respectively. The measured phase shift, φ, is related to the real and imaginary parts of σ^* according to:

$$\varphi = \tan^{-1}\left(\sigma'' / \sigma'\right). \tag{1}$$

Most models for the complex electrical conductivity of a porous material at low frequencies (e.g. less than 100 Hz) are based on charge transfer via a parallel addition of two mechanisms representing (1) an electrolytic contribution via conduction only, without any polarization, through the interconnected pore space (σ_{el}), and (2) a mineral surface contribution via both conduction and polarization within the electrical double layer (EDL) formed at the interfaces of the interconnected pore surface (σ^*_{surf}) (e.g. Vinegar and Waxman, 1984) such that $\sigma^* = \sigma_{el} + \sigma^*_{surf}$. As the electrolyte is essentially unpolarizable at low frequencies, electrolytic conduction is a purely real term so the imaginary component of the overall complex conductivity is derived solely from the mineral surface polarization. The complex surface conductivity associated with the EDL originates from both the fixed surface charges (the Stern layer) and the diffuse layer of charges that exchange with the electrolyte. Based on this parallel conduction model,

6

$$\sigma' = \sigma_{el} + \sigma'_{surf}, \tag{2}$$

$$\sigma'' = \sigma''_{surf}, \tag{3}$$

and for low phase angles, where $\sigma'' << \sigma',$ and $\tan^{-1}(\sigma'/\sigma') \cong \sigma'/\sigma',$

$$\varphi \cong \frac{\sigma''_{surf}}{\sigma_{el}+\sigma'_{surf}} \quad (\varphi < 100 \text{ mrad}). \tag{4}$$

Whereas σ'' represents a direct measure of the polarization of the interconnected pore surface, φ represents the ratio of this polarization to the combined conduction mechanisms within the sample.

The dependence of σ'' on the pore-normalized internal surface area (S_{por}) (e.g., Börner,1992; Weller et al., 2013) and grain size (e.g. Revil and Skold, 2011; Vaudelet et al., 2012) has encouraged many efforts to utilize complex conductivity measurements to predict K (Revil and Florsch, 2010; Slater and Lesmes, 2002b). Furthermore, the dependence of σ'' on σ_w is relatively weak. Weller and Slater (2012) report measurements on 67 sandstone and unconsolidated samples where $\sigma'' \propto \sigma_w^b$ (0.18 < b < 0.55, with the dimensionless exponent b having a mean value of 0.34). Consequently, σ'' is generally considered an excellent indicator of lithologic variability due to (1) its primary dependence on S_{por} and grain size, and (2) its weak dependence on pore fluid conductivity and saturation relative to real conductivity (when dominated by σ_{el}).

HYDROGEOPHYSICAL SETTING

150   The Boise Hydrogeophysical Research Site (BHRS) was established in recognition of the need

151   for improved methods for characterization of permeability distributions in heterogeneous

152   aquifers (Barrash et al., 1999; Clement et al., 1999). The site is situated on a gravel bar beside

153   the Boise River approximately 12 km upstream from downtown Boise, Idaho.

154

155   The unconsolidated sediments of the unconfined aquifer at the BHRS have a thickness of

156   approximately 20 m, and lie above low-permeability red clay (Barrash and Clemo, 2002). A

157   combined drilling and core recovery technique was applied during 1997 and 1998 to construct 18

158   wells at the BHRS. All wells are screened throughout the unconfined sand and cobble aquifer.

159   The central area of the wellfield is comprised of 13 boreholes (Barrash et al., 1999) with a

160   central borehole (A1) surrounded by an inner ring of six boreholes, designated B1 – B6, about 3-

161   4 m from A1 [Figure 1]. A second ring of six boreholes, designated C1 – C6, is positioned about

162   7-10 m from A1, with boreholes in the inner and second rings offset by an angle of

163   approximately 30°. Five additional peripheral boreholes, designated X1 – X5, are positioned

164   around the central area.

165

166   INSERT FIGURE 1 NEAR HERE

167

168   Barrash and Clemo (2002) investigated the subsurface at the BHRS with a neutron logging

169   survey; example $\emptyset$ profiles derived from this analysis are shown in Figure 2. Barrash and Clemo

170   (2002) applied a hierarchical geostatistical approach to the porosity data which supported the

171   recognition of five stratigraphic units (numbered 1 – 5 in depositional sequence order) and

172   recognition of variability and smaller-scale facies within some units. In this stratigraphy, Units 1

173   – 4 are dominated by cobbles, and Unit 5 is a sand channel, which is thickest close to the river,

174   thins away from the river, and pinches out in the center of the wellfield. Of the cobble-

175   dominated units, Units 1 and 3 are very similar and have relatively low $\emptyset$ and variance, while

176   Units 2 and 4 have higher $\emptyset$ and variance (Barrash and Clemo, 2002). This porosity stratigraphy

177   is supported by lithologic stratigraphy based on core (Barrash and Reboulet, 2004).

178

179   INSERT FIGURE 2 NEAR HERE

180

181   A number of geophysical surveys have been previously carried out at the site. Tronicke et al.

182   (2004) gathered a set of GPR measurements from the BHRS, with the transmitter and receiver

183   deployed in C5 and C6, and noted that values of $\emptyset$ derived from an inversion of the GPR data

184   differed in detail from the layered stratigraphy identified by Barrash and Clemo (2002), but a

185   cluster analysis of the inverted GPR data identified clusters with similar values of velocity and

186   attenuation, broadly corresponding to areas with contrasting $\emptyset$ values. Further crosshole GPR

187   analysis was conducted by Ernst et al. (2007) and Irving et al. (2007). Dafflon et al. (2011b)

188   inverted multiple intersecting high-resolution crosshole GPR profiles at the BHRS, and obtained

189   a 3-D distribution of $\emptyset$ values which are in broad agreement with the results of the geostatistical

190   study by Barrash and Clemo (2002).

191

192   The original five unit stratigraphy was extended following the capacitive probe conductivity

193   (CC) well logging outlined in Mwenifumbo et al. (2009). These CC results revealed contrasting

194   electrical properties in one of the cobble units, Unit 2, which led to a new classification of Units

195   2A and 2B (with the upper unit, 2B, having lower electrical conductivity than the lower unit,

196   2A). Figure 3 shows the stratigraphy in well C4 for example. Some of the unit boundaries, in

197   particular those defining Unit 4, are clearly visible in the porosity log, whereas for others the

198   contrast is more subtle. This is further demonstrated by the capacitive probe resistivity (CR) log

199   for well C4, in which the lower boundaries of Units 2A and 2B are also clearly visible.

200

201   INSERT FIGURE 3 NEAR HERE

202

203   In a laboratory study of electrical and hydrologic properties of core samples from the BHRS,

204   Slater et al. (2014) investigated links between sediment grain size distributions and K, and

205   demonstrated the importance of analyzing only the matrix sediment within the cobble

206   framework (i.e., excluding the cobble fraction). They found that, typical of many unconsolidated

207   sediments, the variation in the relaxation time distribution (.001-1000 Hz) between different

208   units was small. No relationship between the relaxation time distribution (frequency response)

209   and pore geometrical properties was observed. Instead, the sediments approximated a constant

210   phase angle behavior from 0.001-10 Hz. However, Slater et al. (2014) did find a relationship

211   between imaginary conductivity (polarization strength) and grain diameter that was subsequently

212   used to test predictions of hydraulic conductivity at this site. They noted that for BHRS

213   sediments, $d_{60(matrix)}$, the grain size for which 60% of a sample of the matrix is smaller, appeared

214   to be a representative grain size for the prediction of K from Kozeny Carman type models,

215   although they emphasized that no single grain size has been shown to be representative for all

216   aquifer materials. Figure 3 includes the profile of particle size for well C4, shown as $d_{60[matrix]}$,

217   obtained from grain size analysis of the sediment cores, after exclusion of cobbles. Subtle

218   changes in $d_{60[matrix]}$ are discernable at the boundaries between Units 2A and 2B, between Units

219   2B and 3, and between Units 3 and 4.

220

221   A high resolution distribution of the six stratigraphic layers in the central region of the BHRS

222   was developed following Barrash and Clemo (2002) and Mwenifumbo et al. (2009) to provide a

223   'ground-truth,' primarily of porosity distributions but also of electrical parameters, against which

224   results of other geophysical surveys can be compared. The distribution is based on a kriged

225   geostatistical model that includes all stratigraphic unit contact elevations in the wells. The model

226   adopts a stationary random field with exponential covariance function with sill 1 m^2 and

227   horizontal correlation length 10 m. The contact between Units 4 and 5 showed drift, which was

228   accounted for in the model. Figure 4 shows an example realization from this approach.

229

230   INSERT FIGURE 4 NEAR HERE

231

232   Hydraulic Conductivity from Multi-Level Slug Tests

233   Recent work by Barrash and Cardiff (2013) using high-resolution data from multi-level slug tests

234   has investigated variation of hydraulic conductivity, *K,* within the BHRS. Details of the slug-test

235   procedures, data quality assessment, and analysis are given in Malama et al. (2011), Cardiff et al.

236   (2011) and Barrash and Cardiff (2013). Figure 5 shows example *K* profiles from a number of

237   wells within the central wellfield.

238

239   INSERT FIGURE 5 NEAR HERE

240

241   Slug tests were run (e.g. Butler, 1998) at two or three different slug heights per zone with highly

242   repeatable results (differences between K from such repeated tests are generally <20% with the

243   occasional poor-quality test excluded from averaging for a given zone) . Values of K identified

244   from the slug tests were corroborated with independent hydraulic tomography results (Cardiff et

245   al., 2013) and clearly show that, although K is not positively correlated with $\emptyset$ or geophysical

246   parameters for all stratigraphic units, K-facies can be identified with multivariate statistical

247   analysis within the established $\emptyset$ -CC stratigraphy (Barrash and Cardiff, 2013). This, along with

248   K-facies boundaries commonly terminating at $\emptyset$ -CC unit contacts, supports the interpretation

249   that K structure is based on sedimentary origins (as are $\emptyset$ and lithology). One of the K-facies has

250   the highest K of all and is generally coincident with Unit 2B, which has the lowest CC of all.

251   Although K-facies within Units 1-2B tend to have a positive association of K with $\emptyset$, K-facies

252   within Units 3-4 tend to have a negative association of K with $\emptyset$ (Barrash and Cardiff, 2013).

253

254   Examination of grain size distribution parameters (including cobble size and percent of the

255   sample, d_{10} and sorting for the whole sample and for the matrix alone) indicate that multiple

256   combinations of these parameters with $\emptyset$ may be associated with similar values of K, but there

257   are tendencies for certain combinations to occur within particular types of K-facies (Barrash and

258   Cardiff, 2013). CC and $\emptyset$ were positively correlated at lower values of K, but negatively

259   correlated at higher values of K. Some negative correlation between CC and the degree of

260   sorting was also observed. The distribution of K in these conglomeratic sediments shows a more

261   complex relationship with geophysical properties than in sand-dominated unconsolidated

262   aquifers where Kozeny-Carman and Archie petrophysics may be more consistently applicable

263   (Barrash and Cardiff, 2013).

264

265   Heterogeneity in K is not great at the BHRS (slightly more than two orders of magnitude for

266   most of the aquifer). The variance of ln K is 0.49, more than three times the ln K variance at the

267   well-studied aquifer of Cape Cod (Wolf et al., 1991), and less than twice that of the aquifer at

268   Borden (Woodbury and Sudicky, 1991). Nevertheless, tracer behavior at the BHRS (Dafflon et

269   al., 2011a; Johnson et al., 2007; Nelson, 2007) is clearly not representative of a homogeneous or

270   simple layered medium in K (or $\emptyset$).

271

272   METHODS

273

274   Our investigation was designed to collect high-resolution complex electrical data with a low and

275   known error structure, suitable for analysis using existing 3-D inversion tools, to provide

276   distributed values of complex electrical parameters for direct comparison with existing

277   stratigraphic models of the BHRS and, where practical, to allow relationships between electrical

278   and hydrologic parameters to be investigated. In the following sections we describe the

279   geophysical measurements, discuss error analysis, summarize the inversion and introduce the

280   statistics used to understand the inversion results.

281

Complex Resistivity Measurements

283 In June 2010 a crosshole complex resistivity survey was conducted at the BHRS. Here we report

284 on analysis of data from wells A1, C2, C3, C4 and C5 (Figure 1). Two electrode arrays, each

285 with 24 stainless steel mesh electrodes spaced 0.61 m apart, were used for measurements

286 between pairs of boreholes in this group of five wells. Well A1 was common to all borehole

287 pairs, and thus the measurement set comprises pairs: A1-C2; A1-C3; A1-C4; A1-C5. This

288 arrangement eliminated the need to remove and relocate one of the electrode arrays whilst still

289 maintaining 3-D coverage over the well cluster.

290

291 As each well is fully screened, electrical contact with the formation is achievable beneath the

292 water table. The top electrode in each well was sited at 846.87 masl (meters above sea level),

293 equivalent to 2.67 m depth at A1. Recognizing the potential impact of current channeling

294 through the water column in the well (e.g. Nimmer et al., 2008), insulating spacers were installed

295 between electrodes to reduce these effects.

296

297 Preliminary field and modeling trials were conducted to determine suitable measurement

298 configurations to meet resolution and data quality objectives. Following these trials, a dipole-

299 dipole arrangement was selected using a 'skip 5' protocol (dipole spacing of 6 electrodes), with

300 forward and reciprocal measurements to allow the error structure to be estimated (Slater et al.,

301 2000) with a current and potential dipole spacing of 3.66 m. For each borehole pair, 922 direct

302 measurements (and the associated reciprocal configuration) were collected using an Iris Syscal

303 Pro instrument (Iris Instruments, Orleans, France). Each measurement set (i.e. one borehole

304 pair) took approximately 110 minutes to collect. Time domain induced polarization (IP)

305   measurements were computed based on a total of 20 windows sampled using a current waveform

306   with 1s on time, 1s off time, 0.12 s delay time, and individual window length of 0.04 s (total

307   window length of 0.8 s).   The 0.12s delay time removes any effect of the instrument's low-pass

308   filter (as reported by Fiandaca et al.,2012) (Iris Instruments, pers. comm., 2015).

309

310   The IP measurements provide a transfer resistance magnitude (or apparent

311   resistivity/conductivity) and an integral chargeabilty, M. Following Mwakanyamale et al.

312   (2012), who used the same instrument settings, we related the complex conductance phase shift

313   (φ) at the current cycle frequency (0.25 Hz) to M through the relationship $\varphi \approx 1.3\,M$, where φ is

314   in mrad, and M is in mV/V. We note that, following the analysis of Kemna et al. (1997), the

315   equivalent scaling factor is 1.5 rather than 1.3 at a corresponding 0.025 Hz current injection

316   frequency.

317

318   *Error Analysis*

319   Quantification of errors is essential for data inversion to ensure: (1) that individual measurements

320   can be appropriately weighted; and (2) that appropriate convergence of the inversion process can

321   be determined. Reciprocal errors, in both resistance magnitude and phase angle, were computed

322   for each dipole configuration and were used to highlight anomalously high errors in both

323   magnitude and phase angle. We adopted error thresholds of 10% and 5 mrad, for magnitude and

324   phase angle respectively (i.e. all data with errors above these thresholds were removed prior to

325   inversion). The computed measurement errors are unsuitable for individual weighting of

326   measurements since they only represent one sample of error for a given configuration. By

327   grouping measurements (ranked by magnitude or phase angle) into 'bins' we can examine trends

328   in errors to allow the development of a simple representative error model. Köestel et al. (2008)

329   used this approach for DC resistivity measurements; Flores Orozco et al. (2012) and

330   Mwakanyamale et al. (2012) extended the method for complex conductivity measurements. We

331   established clear relationships (see Figure 6) between the reciprocal error of both magnitude (ε_R)

332   and phase angle (ε_φ), and the resistance magnitude (R):

333

334        $|\varepsilon_R|$ (in Ohms) $= 0.0147 \, |R|^{0.92}$; $|\varepsilon_\varphi|$ (in mrad) $= 1.637 - 0291 \, \ln(|R|)$.   (5)

335

336   INSERT FIGURE 6 NEAR HERE

337

338   The (almost) linear relationship between $\log_{10}|\varepsilon_R|$ and $\log_{10}|R|$ is a commonly observed error

339   structure (e.g. LaBrecque et al., 1996). In contrast, the reduction in phase angle error, $|\varepsilon_\varphi|$, with

340   increasing $|R|$ highlights the impact of signal strength on the resolution of the IP effect. Measured

341   phase angles were in the range 0 to 15 mrad. As is normal practice (e.g. Slater and Binley,

342   2006), we assume a Gaussian distribution of errors in our inversion process; Figure 7 shows

343   some departure from this model and a slight positive bias.

344

345   INSERT FIGURE 7 NEAR HERE

346

347   *Inversion of Complex Conductivity Measurements*

348   The apparent complex resistance magnitude and phase measurements were inverted to provide 3-

349   D distributions of complex conductivity, expressed in terms of magnitude and phase, using the

350   program *cR3t* (developed by A. Binley at Lancaster University). *cR3t* solves the forward

351   problem using a finite element approximation adopting linear six-node triangular prism elements

352   or four-node tetrahedral elements. A finite element mesh containing 483,448 triangular prism

353   elements and 246,078 nodes was created to model the potential field within the zone of study.

354   The model region extends 130 m laterally (in both directions) and 80 m in depth to account for

355   'infinite' boundary conditions using progressively coarser discretization with increasing distance

356   from the well field. Discretization within the well field zone was approximately 0.4 m (lateral)

357   and 0.2 m (vertical), i.e. three elements per electrode spacing in the vertical.

358

359   Although (four node) tetrahedral elements are computationally more efficient for solving the

360   forward problem, we adopted triangular prism elements for this study because: (1) the electrode

361   positions in the vertical were identical for each well, thus making mesh generation relatively

362   straightforward; and (2) grouping of elements to form parameter blocks is more easily achieved

363   with such a mesh. The latter enhances computational efficiency significantly. For the inverse

364   solution we discretized the region into 42,364 parameter blocks aligned to the forward modeling

365   mesh boundary, with resolution reduced by a factor of exactly 4 in the vertical direction and by

366   approximately 3 for the planar triangulation, as optimized by the mesh generator program.

367

368   The 3-D complex conductivity inversion algorithm used is a 3-D extension of the 2-D algorithm

369   described by Binley and Kemna (2005), and follows the Gauss-Newton method, incorporating an

17

370   iterative refinement of the regularization parameter (α), that minimizes an objective function (Ψ)

371   composed of a data misfit term and a model stabilization term,

372

$$\Psi = \left\| W_d \left(d - f(m) \right) \right\|^2 + \alpha \left\| W_m m \right\|^2, \tag{6}$$

374

375   where W_d is a data weighting matrix associated with individual errors for each measurement, d

376   and f are vectors describing the measured data and forward solution for model vector m

377   respectively, and W_m is a smoothness constraint representing the model weighting matrix which

378   is structured to allow anisotropic smoothing. For the inversions here we adopted a 50:1

379   horizontal:vertical anisotropic smoothing in order to account for the observed horizontal

380   correlation in stratigraphic unit boundaries (e.g. Figure 4); Attwa and Günther (2013) adopted a

381   similar anisotropic smoothing in their inversion of 2D complex conductivity data. For our

382   inversions: data, d, is expressed as an impedance magnitude and phase angle; model vector, m, is

383   expressed as a complex conductivity magnitude (log value) and phase angle. The log

384   transformation constrains the inversion to positive solutions.

385

386   Convergence of the iterative scheme is assumed when the mean of the data misfit component of

387   equation 6 (averaged over the number of measurements) is unity. Given that the formulation

388   expressed in terms of complex conductivity will bias the solution to satisfactory fitting of the

389   magnitude values, as in Kemna (2000), we adopt a 'final phase improvement' scheme, allowing

390   refinement of the parameter phase angles in the final stages of the inversion whilst maintaining

391   the magnitude values determined from the convergence of the first stage of the process.

392

Cluster Analysis

394 In order to assess the value of complex resistivity in differentiating hydrogeological units,

395 despite variation of electrical parameters within each unit, we employed the *k*-means cluster

396 analysis method (MacQueen, 1967), a non-hierarchical partitioning technique which has been

397 successfully used in environmental (e.g. Tronicke et al., 2004; Van Arkel and Kaleita, 2014) and

398 geophysical (e.g. Di Giuseppe et al., 2014) studies. The *k*-means method requires user selection

399 of the number of groups, or clusters, into which a data set should be classified.   Each parameter

400 may also be emphasized or suppressed in its contribution to the identification of structure within

401 the dataset by the chosen method of standardization and by application of a weighting factor (e.g.

402 Gnanadesikan et al., 1995). For a full description of the *k*-means algorithm, see for example,

403 Hartigan and Wong (1979) and Gan et al. (2007).

404 RESULTS

Smoothness Constrained Inverted Models

406 Figure 8 shows the results of the inversion of complex resistivity data. A contrast of only one

407 order of magnitude in real conductivity is apparent; this variation is dominated by the difference

408 between cobble dominated units (Units $1 - 4$) and the sand unit (Unit 5), the latter showing

409 higher real conductivity which is consistent with the observed high $\emptyset$ of these sediments (Figure

410 3). The capacitive probe resistivity logs reported in Mwenifumbo et al. (2009) show similar

411 weak contrast, in their case between 0.5 mS/m and 3 mS/m (-3.3 to -2.5 range in $\log_{10}\sigma'$,

412 expressed in S/m). More subtle variation in real conductivity exists throughout the cobble

413 dominated units, although a distinct contrast is seen at approximately 838 masl and 844 masl (at

414 C5 in Figure 8a, for example). By comparing Figure 8a with Figures 3 and 4 these appear to

415 coincide with the bases of Units 2B and 4, respectively.

416

417   INSERT FIGURE 8 NEAR HERE

418

419 Some lateral variation in real conductivity is seen within the study region, the most notable being

420 the thinning out of the upper conductive zone in the image towards wells C2 and C3 (Figure 8a).

421 Given that we associate this feature with the sand unit (Unit 5), this thinning out is consistent

422 with observed contacts at wells (as illustrated in Figure 4, see also Barrash and Clemo (2002)).

423 Other lateral variation of note is the greater vertical contrast in conductivity (in the lower third of

424 the real and imaginary conductivity images in Figures 8b and 8c between wells C4 and C5.

425 However, this cannot be explained by the contrast in $\emptyset$ because these contrasts are all similar at

426 about 835 masl in wells C3 and C2 also (Figure 2).

427

428 Generally weak variation in computed phase angle exists (Figure 8c), although contrasts are

429 clearly visible. Figure 9 shows the distribution of normalized misfit for the measurements, i.e.

430 the difference between measured and modeled phase angle relative to the assumed error (from

431 equation 5). Such a distribution should ideally be Gaussian with a zero mean and unit variance.

432 The modeled phase angles are typically around 2 to 4 mrad, which is consistent with those

433 observed from complex conductivity measurements on reconstituted samples from the site

434 (Slater et al., 2014). A low phase angle appears to be associated with the sand unit (Unit 5). The

435 relatively weak variation in phase angle will be due in part to the subtle contrast in sediment

436 properties but also due to the weaker signal to noise ratio of measured phase angle in comparison

437 to resistance magnitude, despite great care in data acquisition and rigorous treatment of phase

438 angle data errors (Figures 6 and 7).   However it is the imaginary conductivity that uniquely

439 resolves polarization and, despite the weak variation in phase angle, this property helps

440 emphasize contrasts within the study region (Figure 8b). In particular, the lower third of the

441 imaged region shows distinctly greater polarization than the upper section. Note also the very

442 low polarization associated with the sand unit near boreholes C4 and C5.

443

444   INSERT FIGURE 9 NEAR HERE

445

446 Barrash and Clemo (2002) used the porosity logs (e.g., Figure 2) to develop probability density

447 functions for unit-specific $\emptyset$ across the wellfield. Their analysis reveals contrasts in the

448 distributions, for example greater variance of $\emptyset$ in Units 2 and 4, in comparison to Units 1 and 3

449 (Figure 5 in Barrash and Clemo,2002)). Here we could apply the same analysis using image

450 voxel values at well locations. However, these would be limited to areas of higher imaging

451 resolution and thus would be somewhat biased. Instead we use one of the unit boundary

452 realizations (Figure 4) to delineate the complex resistivity image and thus allow the formation of

453 unit-specific complex resistivity distributions. Figure 10 shows these distributions, expressed in

454 terms of real conductivity and phase angle, for Units 2A, 2B, 3, 4 and 5. Examining the real

455 conductivity, we see a smaller variance in Unit 3 compared to Units 4 and 5, as in Barrash and

456 Clemo (2002). We also note that Units 2A and 2B combined (equivalent to Unit 2 in Barrash

457 and Clemo, 2002) also have larger variance than Unit 3. However, interestingly, given the newer

458 Unit 2 subdivision, Units 2B and Unit 3 are relatively indistinguishable in terms of real

459 conductivity distributions although a subtly lower mean conductivity is apparent for Unit 2B

460   when compared to Unit 3, which is consistent with the capacitive probe conductivity logs of

461   Mwenifumbo et al. (2009) noted earlier. The phase angle distributions also show contrasts across

462   some units (e.g. Units 3 and 4), and again with close similarity between Unit 2B and Unit 3.

463

464   INSERT FIGURE 10 NEAR HERE

465

466   The above comparison assumes that each computed electrical parameter value within the image

467   is equally resolvable, however, we note that variations in spatial sensitivity are inherent in any

468   electrical imaging method. Nevertheless, given the relatively horizontal stratigraphy inferred

469   from the analysis of unit contacts (e.g. Figure 4), any bias in the distributions (due to greater

470   smoothing between electrode locations, for example) is likely to be reasonably equal across all

471   units.

472

473   *Cluster Analysis*

474   The inversion results were projected from the irregular mesh used in the inversion to orthogonal

475   grids (80 x 40 x 60 elements) with a resolution selected as a compromise between computational

476   complexity and excessive smoothing. Only the inverted results within the volume bounded by

477   the electrode arrays were used. Five parameter values at each voxel were standardized by unit-

478   normalizing to a value between 0 and 1, representing the maximum and minimum values for

479   each parameter. The parameters consisted of the x, y and z spatial coordinates together with two

480   parameters representing complex conductivity expressed either as phase angle and the logarithm

481   of magnitude, or as the logarithms of both the imaginary and real components. Cluster analysis

482   was carried out using either five or six clusters; these values were chosen because application of

483   multiple analyses with identical values for all other parameters showed greatest consistency with

484   five clusters, slightly reduced consistency with six clusters, and poor consistency with four or

485   seven clusters. Furthermore, analyses with five or six clusters allowed comparisons to be made

486   with previous interpretations of BHRS stratigraphy based on $\emptyset$, lithology, and CC (Barrash and

487   Clemo, 2002; Barrash and Reboulet, 2004; Mwenifumbo et al., 2009). Each identified cluster

488   could include any non-zero proportion of the total number of voxels in the grid, and could have

489   irregular and discontinuous boundaries.

490

491   For selected cluster analyses, using five or six clusters, the nonparametric Kolmogorov-Smirnov

492   test (Conover, 1999) was applied to determine whether the 3-D distribution of σ' within each

493   identified cluster differs significantly from the distribution within every other cluster, and this

494   was repeated to test for significantly different distributions of σ''. In all cases, the null

495   hypothesis that the distributions do not differ can be rejected ($p < 10^{-4}$).

496

497   Figure 11 shows three-dimensional representations of our five-cluster analysis using DC

498   conductivity only (Figure 11a), and using both DC conductivity and IP data (Figure 11b). Only

499   subtle differences are noticeable, highlighting that the lithologic boundary differentiation is most

500   strongly influenced by the DC conductivity. Example cluster analysis results are shown in

501   Figures 12 and 13 for extracted profiles at well locations C4 and B4, respectively. Well B4 (for

502   location see Figure 1) was selected as an example between the electrode array locations (where

503   resolution of the electrical imaging is weaker). Figures 12 and 13 show the results for five- and

504   six-unit cluster analysis, together with the previously defined unit boundaries. In both examples,

505   clusters K3 and K4 for the five-cluster model closely represent clusters K3 to K5 in the six-

506   cluster model, revealing that this interval is the zone of weakest contrast. The six-cluster model,

507   in both cases, shows close similarity to the unit boundaries (shown as units U1 to U5 in Figures

508   12 and 13). Although the boundaries do not match perfectly, features such as the thinning of

509   Unit 4 from well B4 to C4 are clearly visible. The boundary between Unit 2B and 3, although

510   subtle in terms of real conductivity, is well resolved in both cases, supporting the earlier

511   comments about differences in electrical conductivity between these two units. A distinct

512   contrast in imaginary conductivity is seen at the Unit 2A-Unit 2B boundary in both cases.

513

514   INSERT FIGURE 11 NEAR HERE

515   INSERT FIGURE 12 NEAR HERE

516   INSERT FIGURE 13 NEAR HERE

517

518   DISCUSSION

519

520   In this study we have inverted cross-borehole time-domain measurements of complex electrical

521   conductivity, but our results show a very close correspondence between the real and imaginary

522   components of the 3-D distributed values of complex conductivity (Figure 8). We note, however,

523   that the equipment required to record time-domain complex electrical measurements requires

524   little additional time to deploy (relative to a frequency-domain spectral IP survey), over an

525   equivalent DC survey.

526

K Information

527

528 The aquifer at the BHRS site has fairly low heterogeneity in *K*, with a range of 6.4×10^{-5} – $1.6 \times$

529 10^{-2} ms^{-1} (Barrash and Cardiff, 2013) and a lack of strong overall correlation between *K* and $\emptyset$

530 (Cardiff et al., 2011). Indeed the *K* distribution has both positive and negative associations with

531 $\emptyset$ in lower and upper portions of the stratigraphy, respectively (Barrash and Cardiff, 2013;

532 Cardiff et al., 2013) indicating that only in portions of the coarse unconsolidated sediments at the

533 BHRS is *K* more strongly influenced by overall $\emptyset$ than by the surface area and tortuosity of the

534 pore channels (which control S_{por}). We suggest that the additional information in the imaginary

535 component of IP measurements is more likely to be correlated to S_{por} in consolidated materials

536 such as sandstones in which the surface area of pores and channels can vary almost

537 independently of $\emptyset$. The lack of variability in field scale σ'' limits the estimation of subtle spatial

538 variation of S_{por}, and hence K, using the relationships developed by, for example, Börner and

539 Schön (1991), Börner et al. (1996), Slater and Lesmes (2002b) and Weller et al. (2010).

540 However, in order to investigate IP-derived estimates of hydraulic conductivity we draw upon

541 the recent relationship empirically derived by Weller et al. (2015) from a dataset of 22

542 unconsolidated laboratory samples. They propose the link between permeability, *k* (in m^2) and

543 complex electrical conductivity (equation 24 in Weller et al., 2015) as:

544

$$k = \frac{3.47 \times 10^{-16}\sigma^{1.11}}{\sigma''^{2.41}}, \tag{7}$$

545

546   assuming a fluid conductivity σ_w=100mS/m.   Fluid electrical conductivity at the site is typically

547   20mS/m, however, the two electrical parameters in equation 7 are easily scaled to reflect this

548   (see for example, Weller et al., 2015).

549

550   Figure 14 shows example profiles of hydraulic conductivity computed using equation 7, using

551   complex conductivity values from the inverse model (Figure 8).   The profiles in Figure 14 show

552   multi-level slug test estimates of hydraulic conductivity for comparison.   From the profiles in

553   Figure 14, the difference between values from the hydrogeological and geophysical

554   measurements is typically within an order of magnitude. The correspondence is closer in the

555   lower portion of the stratigraphy where K and porosity are related, although in the upper units of

556   B3 and B4 the low polarization results in a much higher estimate of K - where K and porosity

557   are poorly related (Barrash and Cardiff, 2013). The differentiation of subtle changes in hydraulic

558   conductivity is, however, more challenging. Figure 14 shows similar locations of some smaller-

559   scale features (lenses) in each well but with variable polarity in slug data vs K estimates from

560   equation 7 because in-situ measurements reflect non-uniform dependence of slug K on porosity,

561   grain size distribution, shape and packing (detailed in Barrash and Cardiff, 2013).

562

563   INSERT FIGURE 14 NEAR HERE

564

565   Slater et al. (2014) found that relationships between σ'', effective grain size (best represented by

566   the grain diameter for which 60% of the sample is finer) and K could be identified from

567   controlled laboratory-scale measurements on 12 samples spanning the five units originally

568   identified at the BHRS (Barrash and Clemo, 2002; Barrash and Reboulet, 2004). In these

569 reconstituted samples, K only varied by about a factor of 3 and thus the full range of K at the site

570 was not captured. The ability to identify electrical-hydraulic relationships over such a narrow

571 range of K would on its own appear to encourage field-scale IP measurements for mapping

572 hydrogeological structures in such settings. Findings from this field study tend to support this

573 conclusion, however, contrasts in field-based estimates from inversion may be more difficult to

574 determine, despite considerable efforts to minimize noise and careful estimation of the error

575 structure within the measurements.

576

577 *Units and Multi-scale Structure*

578 Our attempts to use the geophysical data for the identification of hydrogeological units has

579 revealed only marginal additional information within σ'' beyond that within σ' at the BHRS.

580 We note the ability of the *k*-means cluster analysis method to simplify the 3-D distribution of σ',

581 by identifying a predetermined number of regions approximated as horizontal layers.

582 Application of the Kolmogorov-Smirnov test has shown that the empirical distribution of σ'

583 values in each of the identified layers is significantly different from that of every other layer,

584 confirming that the layered structures identified through cluster analysis relate to geophysical

585 differences, despite the relatively high emphasis given to the vertical dimension in both the

586 inversion and clustering procedures. Vertical 1-D samples through the simplified layered

587 structure identified by the cluster analysis, such as at the positions of boreholes B4 and C4

588 (Figures 12-13), show good correlation between the layer boundaries and the boundaries

589 between the stratigraphic units. The delineation of the Unit 2A/Unit 2B boundary is noticeably

590 emphasized by the σ'' profile (see Figures 12-13). Results of the cluster analysis of the 3-D

591   inversion of σ' measurements are broadly supportive of the multi-scale heterogeneity affecting

592   hydraulic, lithologic, and geophysical parameters which has been demonstrated in the

593   sedimentary structure of the site (Barrash and Clemo, 2002; Barrash and Reboulet, 2004), and

594   recognition of two types of electrical-porosity (and dielectric-porosity) behavior evident in the

595   subdivision of Unit 2 into Units 2A and 2B (Mwenifumbo et al. 2009; Ernst et al., 2007; Irving

596   et al., 2007; Dafflon et al., 2011b) . Observation of $\emptyset$ and CC logs and analysis of correlation

597   between $\emptyset$ and CC, show strong correlation at the stratigraphic unit scale but highly variable

598   weak to strong correlation at the sub-unit scale (Figure 14 here and Barrash and Cardiff, 2013).

599

600   The strong influence of the magnitude of complex conductivity on the imaginary conductivity

601   appears to mask much of the apparent variation in IP when viewed in terms of phase angle.

602   However, we note that, for example, Units 3 and 2B appear to show similar real conductivity, but

603   differ noticeably in phase angle (Figure 10). We have focused our analysis and interpretation

604   here using σ' and σ'' as measures of conduction and polarization, however, future studies may

605   seek to establish grounds for incorporating the phase angle as a means of discriminating

606   hydrogeological units.

607

608   *Frequency-related IP Properties*

609   Our complex electrical measurements were recorded in the time domain, with a fixed step

610   duration, converted to equivalent frequency-domain measurements recorded at a single

611   frequency (in this case 0.25 Hz). The phase components of the complex electrical resistance

612   values which were used in the inversion were derived from a simple relationship between phase

613 and normalized chargeability. Although the validity of this relationship has been demonstrated

614 in several studies (e.g. Kemna et al., 1997; Mwakanyamale et al., 2012), we speculate that lower

615 correlation between the magnitude and phase components might be observed if complex

616 electrical measurements were directly recorded in the frequency domain as done in the

617 laboratory. Other studies have investigated frequency-domain measurements of induced

618 polarization in porous materials recorded over a broad spectrum of frequencies, with attempts to

619 link a frequency-related property of induced polarization to physical properties of the material.

620

621 An overview of this spectral induced polarization (SIP) approach in near-surface investigations

622 has been provided by Kemna et al. (2012), and identification of mechanistic relationships

623 between physical properties which control hydraulic conductivity and SIP parameters continues

624 to be an active and promising area of research (Florsch et al., 2012; Revil et al., 2015). However,

625 as previously noted, this site is characterized by sediments that show very small differences in

626 frequency-related properties between the units, suggesting that SIP studies will show the same

627 limitations as IP methods at $\emptyset$ dominated sites with low heterogeneity in hydraulic characteristics

628 of interest. We also note recent efforts to analyze time series of time-domain IP data in an

629 attempt to remove superposition of charging cycles (Fiandaca et al., 2013). Such approaches,

630 although currently limited to 2-D analysis and specific polarization models, may offer greater

631 ability to resolve more subtle contrasts in complex conductivity, especially where there is

632 evidence for additional (i.e., not K-C) petrophysics that is not dominated by $\emptyset$ (e.g., Barrash and

633 Cardiff, 2013; Morin, 2006).

634

635

636   CONCLUSIONS

637

638   Our study has demonstrated that the field-scale IP approach may be suitable for providing

639   estimates of hydraulic conductivity in coarse grained aquifers but somewhat limited for the

640   resolution of small-scale (e.g., lenses vs layers, Figure 14) contrasts in hydraulic conductivity

641   variation. Despite the acquisition of high quality complex electrical measurements, and careful

642   handling in the inversion procedure of the estimated data errors, it is clear that low contrast in K

643   at the BHRS resulted in relatively low structural resolution based on the distribution of induced

644   polarization parameters.

645

646   Although our investigation was unsuccessful in providing a clear description of the distribution

647   of K in the central region of the BHRS, a site with (a) low to moderate K heterogeneity typical of

648   many high-energy coarse unconsolidated aquifers, and (b) multiple relations between K and $\emptyset$,

649   we have shown that the purely conductive component of our complex measurements has

650   provided supporting evidence for a stratigraphic structure including low-contrast features

651   identified in previous investigations – even though the energy storage component has provided

652   limited additional information at this site. We have shown the value of k-means cluster analysis

653   in simplifying and identifying structure from complicated parameter distributions.

654

655   Our results have highlighted the potential danger of interpreting IP images from similar

656   environments independently of other data. In many highly permeable aquifer systems, a level of

657   heterogeneity of hydraulic properties that can influence flow and solute transport may be

658   extremely subtle from an electrical geophysics perspective. Obtaining high quality IP

659 measurements is not straightforward and the signal-to-noise in polarization measurements may

660 limit its use in noisy and/or poorly controlled settings. However, where significant contrasts in

661 sediment properties are expected, we believe that IP has significant potential, e.g. in

662 identification of hydrogeologic boundaries, perhaps at multiple scales.

663

664 Finally, we note that our analysis has employed a commonly used smoothness-based inversion

665 for our geophysical data. We adopted this as a means of evaluating the value of IP using widely

666 acceptable procedures. However, one may envisage greater resolution of IP contrasts at sites,

667 such as the BHRS, where other *a priori* information is used to constrain the inversion. We

668 expect to see greater awareness and application of this approach in future studies.

669 ACKNOWLEDGMENTS

670

677

678

679   REFERENCES

680

681   Archie, G.E., 1942. The electrical resistivity log as an aid in determining some reservoir

682   characteristics. Transactions of the American Institute of Mining and Metallurgical

683   Engineers, 146: 54-62.

684   Attwa, M., Günther, R., 2013. Spectral induced polarization measurements for predicting the

685   hydraulic conductivity in sandy aquifers, Hydrology and Earth System Sciences, 17:

686   4079–4094.

687   Barrash, W., Reboulet, E.C., 2004. Significance of porosity for stratigraphy and textural

688   composition in subsurface coarse fluvial deposits, Boise Hydrogeophysical Research

689   Site. Geological Society of America Bulletin, 116: 1059-1073.Barrash, W., Cardiff,

690   M.,2013. Hydraulic conductivity distribution from multi-level slug tests and multivariate

691   facies associations in a conglomerate fluvial aquifer, Boise Hydrogeophysical Research

692   Site. Tech. Rep. BSU CGISS 13-03, 71 pp., Boise State Univ., Boise, USA.

693   Barrash, W., Clemo, T., 2002. Hierarchical geostatistics and multifacies systems: Boise

694   Hydrogeophysical Research Site, Boise, Idaho. Water Resources Research, 38(10).

695   Barrash, W., Clemo, T., Fox, J.J., Johnson, T.C., 2006. Field, laboratory, and modeling

696   investigation of the skin effect at wells with slotted casing, Boise Hydrogeophysical

697   Research Site. Journal of Hydrology, 326: 181–198.

698   Barrash, W., Clemo, T., Knoll, M.D., 1999. Boise Hydrogeophysical Research Site (BHRS):

699   Objectives, design, initial geostatistical results. Proceedings of the Symposium on the

700   Application of Geophysics to Engineering and Environmental Problems, 389-398 pp.

701   Bentley, L.R., Gharibi, M., 2004. Two- and three-dimensional electrical resistivity imaging at a

702   heterogeneous remediation site. Geophysics, 69(3): 674-680.

703   Binley, A., Kemna, A., 2005. DC Resistivity and Induced Polarization Methods. In: Rubin, Y.,

704   Hubbard, S.S. (Eds.), Hydrogeophysics. Water Science and Technology Library.

705   Springer, pp. 523.

706   Börner, F.D., 1992. Complex conductivity measurements of reservoir properties. In:

707   Worthington, P.F., Chardaire-Riviere, C. (Eds.), Proceedings of the Third European Core

708   Analysis Symposium. Harwood Academic, Newark, pp. 359-386.

709   Börner, F.D., Schön, J.H., 1991. A relation between the quadrature component of electrical

710   conductivity and the specific surface area of sedimentary rocks. The Log Analyst, 32:

711   612–613.

712   Börner, F.D., Schopper, J.R., Weller, A., 1996. Evaluation of transport and storage properties in

713   the soil and groundwater zone from induced polarization measurements. Geophysical

714   Prospecting, 44(4): 583-601.

715   Brauchler, R. et al., 2010. Cross-well slug interference tests: An effective characterization

716   method for resolving aquifer heterogeneity. Journal of Hydrology, 384(1–2): 33-45.

717   Butler, J.J., 1998. The design, performance, and analysis of slug tests. CRC Press, Boca Raton,

718   FL, 262 pp.

719   Cardiff, M., Barrash, W., Kitanidis, P.K., 2012. A field proof-of-concept of aquifer imaging

720   using 3-D transient hydraulic tomography with modular, temporarily-emplaced

721   equipment. Water Resources Research, 48(5): W05531.

722   Cardiff, M., Barrash, W., Kitanidis, P.K., 2013. Hydraulic conductivity imaging from 3-D

723   transient hydraulic tomography at several pumping/observation densities. Water

724   Resources Research, 49: 1-16.

725   Cardiff, M. et al., 2009. A potential-based inversion of unconfined steady-state hydraulic

726   tomography. Ground Water, 47(2): 259-270.

727   Cardiff, M., Barrash, W., Thoma, M., Malama, B., 2011. Information content of slug tests for

728   estimating hydraulic properties in realistic, high-conductivity aquifer scenarios. Journal

729   of Hydrology, 403(1-2): 66-82.

730   Cassiani, G., Bruno, V., Villa, A., Fusi, N., Binley, A.M., 2006. A saline trace test monitored via

731   time-lapse surface electrical resistivity tomography. Journal of Applied Geophysics,

732   59(3): 244-259.

733   Charbeneau, R.J., 1999. Groundwater hydraulics and pollutant transport. Prentice Hall, Upper

734   Saddle River, NJ, 593 pp.

735   Clement, W.P. et al., 1999. Geophysical surveys across the Boise Hydrogeophysical Research

736   Site to determine geophysical parameters of a shallow, alluvial aquifer. Proceedings of

737   the Symposium on the Application of Geophysics to Engineering and Environmental

738   Problems, 399-408 pp.

739   Conover, W.J., 1999. Practical nonparametric statistics. John Wiley, New York, 592 pp.

740   Dafflon, B., Barrash, W., Cardiff, M., Johnson, T.C., 2011a. Hydrological parameter estimations

741   from a conservative tracer test with variable-density effects at the Boise

742   Hydrogeophysical Research Site. Water Resources Research, 47(12): W12513.

743   Dafflon, B., Irving, J., Barrash, W., 2011b. Inversion of multiple intersecting high-resolution

744   crosshole GPR profiles for hydrological characterization at the Boise Hydrogeophysical

745   Research Site. Journal of Applied Geophysics, 73(4): 305-314.

746   Di Giuseppe, M.G., Troiano, A., Troise, C., De Natale, G., 2014. k-Means clustering as tool for

747   multivariate geophysical data analysis. An application to shallow fault zone imaging.

748   Journal of Applied Geophysics, 101: 108-115.

749   Diem, S., Vogt, T., Hoehn, E., 2010. Räumliche Charakterisierung der hydraulischen

750   Leitfähigkeit in alluvialen Schotter-Grundwasserleitern: Ein Methodenvergleich.

751   Grundwasser, 15: 241–251.

752   Doetsch, J., Linde, N., Pessognelli, M., Green, A.G., Günther, T., 2012. Constraining 3-D

753   electrical resistance tomography with GPR reflection data for improved aquifer

754   characterization. Journal of Applied Geophysics, 78: 68-76.

755   Ernst, J.R., Green, A.G., Maurer, H., Holliger, K., 2007. Application of a new 2D time-domain

756   full-waveform inversion scheme to crosshole radar data. Geophysics, 72(5): J53-J64.

757   Fiandaca, G., Auken, E., Vest Christiansen, A., Gazoty, A., 2012. Time-domain-induced

758   polarization: Full-decay forward modeling and laterally constrained inversion of Cole-

759   Cole parameters. Geophysics, 77(3): E213-E225.

760   Fiandaca, G., Ramm, J., Binley, A., Gazoty, A., Vest Christiansen, A., Auken, E. 2013.

761   Resolving spectral information from time domain induced polarization data through 2-D

762   inversion. Geophysical Journal International, 192: 631-646.

763   Flores Orozco, A., Kemna, A., Zimmermann, E., 2012. Data error quantification in spectral

764   induced polarization imaging. Geophysics, 77(3): E227-E237.

765   Florsch, N., Camerlynck, C., Revil, A., 2012. Direct estimation of the distribution of relaxation

766   times from induced-polarization spectra using a Fourier transform analysis. Near Surface

767   Geophysics, 10(6): 517-531.

768   Gan, G., Ma, C., Wu, J., 2007. Data clustering, theory, algorithms, and applications. Statistics

769   and applied probability. Society for Industrial and Applied Mathematics, Philadelphia,

770   488 pp.

771   Gnanadesikan, R., Kettenring, J.R., Tsao, S.L., 1995. Weighting and selection of variables for

772   cluster analysis. Journal of Classification, 12(1): 113-136.

773   Griffiths, D.H., Turnbull, J., 1985. A multi-electrode array for resistivity surveying. First Break

774   3(7): 16-20.

775   Hartigan, J.A., Wong, M.A., 1979. Algorithm AS 136: A K-Means Clustering Algorithm.

776   Journal of the Royal Statistical Society. Series C (Applied Statistics), 28(1): 100-108.

777   Hördt, A., Blaschek, R., Kemna, A., Zisser, N., 2007. Hydraulic conductivity estimation from

778   induced polarisation data at the field scale - the Krauthausen case history. Journal of

779   Applied Geophysics, 62(1): 33-46.

780   Hördt A., Blaschek R., Binot F., Druiventak A., Kemna A., Kreye P., Zisser N. 2009. Case

781   histories of hydraulic conductivity estimation with induced polarisation at the field scale.

782   *Near-Surface Geophysics*, 7(5-6): 529–545.

783   Irving, J.D., Knoll, M.D., Knight, R.J., 2007. Improving crosshole radar velocity tomograms: A

784   new approach to incorporating high-angle traveltime data. Geophysics, 72(4): J31-J41.

785   Jardani, A., Revil, A., Dupont, J.P., 2013. Stochastic joint inversion of hydrogeophysical data for

786   salt tracer test monitoring and hydraulic conductivity imaging. Advances in Water

787   Resources, 52: 62-77.

788   Johnson, T.C., Routh, P.S., Barrash, W., Knoll, M.D., 2007. A field comparison of Fresnel zone

789   and ray-based GPR attenuation-difference tomography for time-lapse imaging of

790   electrically anomalous tracer or contaminant plumes. Geophysics 72(2): G21–G29.

791   Kemna, A., 2000. Tomographic inversion of complex resistivity: Theory and application, Ph.D.

792   thesis. Der Andere Verlag, Osnabrück, 176 pp.

793   Kemna, A. et al., 2012. An overview of the spectral induced polarization method for near-surface

794   applications. Near Surface Geophysics, 10(6): 453-468.

795   Kemna, A., Binley, A., Slater, L.D., 2004. Crosshole IP imaging for engineering and

796   environmental applications. Geophysics, 69(1): 97-107.

797   Kemna, A., Räkers, E., Binley, A., 1997. Application of complex resistivity tomography to field

798   data from a kerosene-contaminated site, 3rd Meeting of the Environmental and

799   Engineering Geophysics Society, Aarhus, pp. 151-154.

800   Köestel, J., Kemna, A., Javaux, M., Binley, A., Vereecken, H., 2008. Quantitative imaging of

801   solute transport in an unsaturated and undisturbed soil monolith with 3-D ERT and TDR.

802   Water Resources Research, 44(12).

803   Koltermann, C.E., Gorelick, S.M., 1995. Fractional packing model for hydraulic conductivity

804   derived from sediment mixtures. Water Resources Research, 31(12): 3283-3297.

805   LaBrecque, D.J., Miletto, M., Daily, W., Ramirez, A., Owen, E., 1996. The effects of noise on

806   Occam's inversion of resistivity tomography data. Geophysics, 61(2): 538-548.

807   Loke, M.H., Chambers, J.E., Rucker, D.F., Kuras, O., Wilkinson, P.B., 2013. Recent

808   developments in the direct-current geoelectrical imaging method. Journal of Applied

809   Geophysics, 95(0): 135-156.

810   MacQueen, J., 1967. Some methods for classification and analysis of multivariate observations,

811   5th Berkeley symposium on mathematical statistics and probability. University of

812   California Press, Berkeley, pp. 281-297.

813   Malama, B., Kuhlman, K.L., Barrash, W., Cardiff, M., Thoma, M., 2011. Modeling slug tests in

814   unconfined aquifers taking into account water table kinematics, wellbore skin and inertial

815   effects. Journal of Hydrology, 408(1-2): 113-126.

816   Morin, R.E., 2006. Negative correlation between porosity and hydraulic conductivity in sand-

817   and-gravel aquifers at Cape Cod, Massachusetts, USA. Journal of Hydrology, 316: 43-52.

818   Mwakanyamale, K., Slater, L.D., Binley, A., Ntarlagiannis, D., 2012. Lithologic imaging using

819   complex conductivity: Lessons learned from the Hanford 300 Area. Geophysics, 77(6):

820   E397-E409.

821   Mwenifumbo, C.J., Barrash, W., Knoll, M.D., 2009. Capacitive conductivity logging and

822   electrical stratigraphy in a high-resistivity aquifer, Boise Hydrogeophysical Research

823   Site. Geophysics, 74(3): E125-E133.

824   Nelson, G., 2007. Deterministic modeling of bromide tracer transport during the tracer/time-

825   lapse radar imaging test at the Boise hydrogeophysical research site in August, 2001.

826   M.S. Thesis, Boise State University.

827   Nimmer, R.E., Osiensky, J.L., Binley, A.M., Williams, B.C., 2008. Three-dimensional effects

828   causing artifacts in two-dimensional, cross-borehole, electrical imaging. Journal of

829   Hydrology, 359(1-2): 59-70.

830

831   Reboulet, E.C. and Barrash, W., 2003, Core, grain-size, and porosity data from the Boise

832   Hydrogeophysical Research Site, Boise, Idaho: BSU CGISS Technical Report, 03-02,

833   Boise State University, Boise, ID, 84 p.Revil, A., Florsch, N., 2010. Determination of

834   permeability from spectral induced polarization in granular media. Geophysical Journal

835   International, 181: 1480-1498.

836   Revil, A., Skold, M., 2011. Salinity dependence of spectral induced polarization in sands and

837   sandstones. Geophysical Journal International, 187(2): 813-824.

838   Revil, A., Binley, A., Mejus, L., Kessouri, P. 2015. Predicting permeability from the

839   characteristic relaxation time and intrinsic formation factor of complex conductivity

840   spectra. Water Resources Research, 51(8): 6672–6700

841   Slater, L.D., Barrash, W., Montrey, J., Binley, A., 2014. Electrical-hydraulic relationships

842   observed for unconsolidated sediments in the presence of a cobble framework. Water

843   Resources Research. 50(7): WR014631

844   Slater, L.D., Binley, A., 2006. Synthetic and field-based electrical imaging of a zerovalent iron

845   barrier: Implications for monitoring long-term barrier performance. Geophysics, 71(5):

846   B129-B137.

847   Slater, L.D., Binley, A.M., Daily, W., Johnson, R., 2000. Cross-hole electrical imaging of a

848   controlled saline tracer injection. Journal of Applied Geophysics, 44(2-3): 85-102.

849   Slater, L.D., Glaser, D.R., 2003. Controls on induced polarization in sandy unconsolidated

850   sediments and application to aquifer characterization. Geophysics, 68(5): 1547-1558.

851   Slater, L.D., Lesmes, D., 2002a. IP interpretation in environmental investigations. Geophysics,

852   67(1): 77-88.

853   Slater, L.D., Lesmes, D.P., 2002b. Electrical-hydraulic relationships observed for unconsolidated

854   sediments. Water Resources Research, 38(10): WR001075

855 Stummer, P., Maurer, H., Horstmeyer, H., Green, A.G., 2002. Optimization of DC resistivity

856 data acquisition: real-time experimental design and a new multielectrode system.

857 Geoscience and Remote Sensing, IEEE Transactions on, 40(12): 2727-2735.

858 Sudicky, E.A., 1986. A natural gradient experiment on solute transport in a sand aquifer: Spatial

859 variability of hydraulic conductivity and its role in the dispersion process. Water

860 Resources Research, 22(13): 2069-2082.

861 Tronicke, J., Holliger, K., Barrash, W., Knoll, M.D., 2004. Multivariate analysis of cross-hole

862 georadar velocity and attenuation tomograms for aquifer zonation. Water Resources

863 Research, 40(1).

864 Van Arkel, Z., Kaleita, A.L., 2014. Identifying sampling locations for field-scale soil moisture

865 estimation using K-means clustering. Water Resources Research, 50(8): 7050-7057.

866 Vaudelet, P., Revil, A., Schmutz, M., Franceschi, M., Bégassat, P., 2011. Induced polarization

867 signatures of cations exhibiting differential sorption behaviors in saturated sands. Water

868 Resources Research, 47(2): W02526.

869 Vinegar, H.J., Waxman, M.H., 1984. Induced polarization of shaly sands. Geophysics, 49(8):

870 1267-1287.

871 Weller, A., Slater, L., Nordsiek, S., Ntarlagiannis, D. 2010. On the estimation of specific surface

872 per unit pore volume from induced polarization: A robust empirical relation fits multiple

873 data sets. Geophysics, 75(4): WA105-WA112.

874   Weller, A., Slater, L., 2012. Salinity dependence of complex conductivity of unconsolidated and

875   consolidated materials: Comparisons with electrical double layer models. Geophysics,

876   77(5): D185-D198.

877   Weller, A., Slater, L., Nordsiek, S., 2013. On the relationship between induced polarization and

878   surface conductivity: Implications for petrophysical interpretation of electrical

879   measurements. Geophysics, 78(5): D315-D325.

880   Weller, A., Slater, L., Binley, A., Nordsiek, S., and Xu, S., 2015. Permeability prediction based

881   on induced polarization: Insights from measurements on sandstone and unconsolidated

882   samples spanning a wide permeability range. Geophysics, 80(2): D161-D173.

883   Wolf, S.H., Celia, M.A., Hess, K.M., 1991. Evaluation of hydraulic conductivities calculated

884   from multiport-permeameter measurements. Ground Water, 29(4): 516-525.

885   Woodbury, A.D., Sudicky, E., 1991. The geostatistical characteristics of the Borden aquifer.

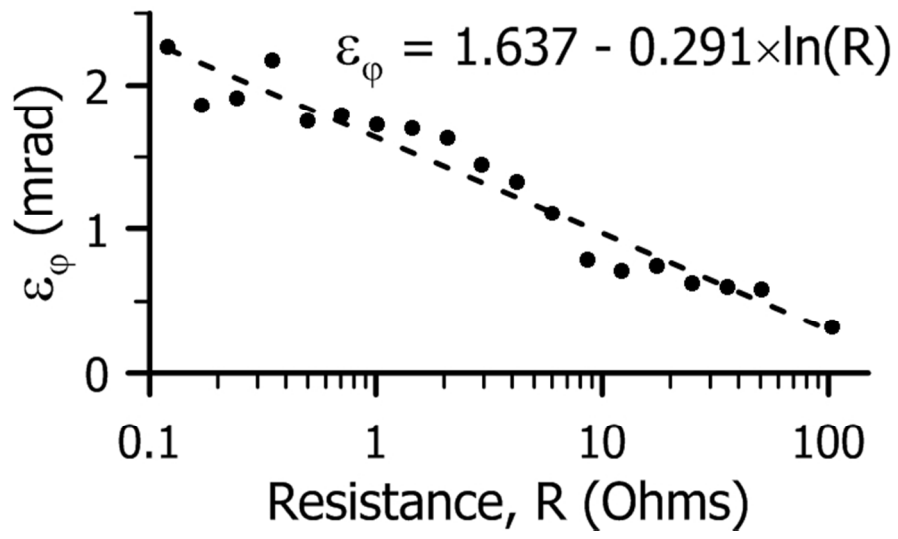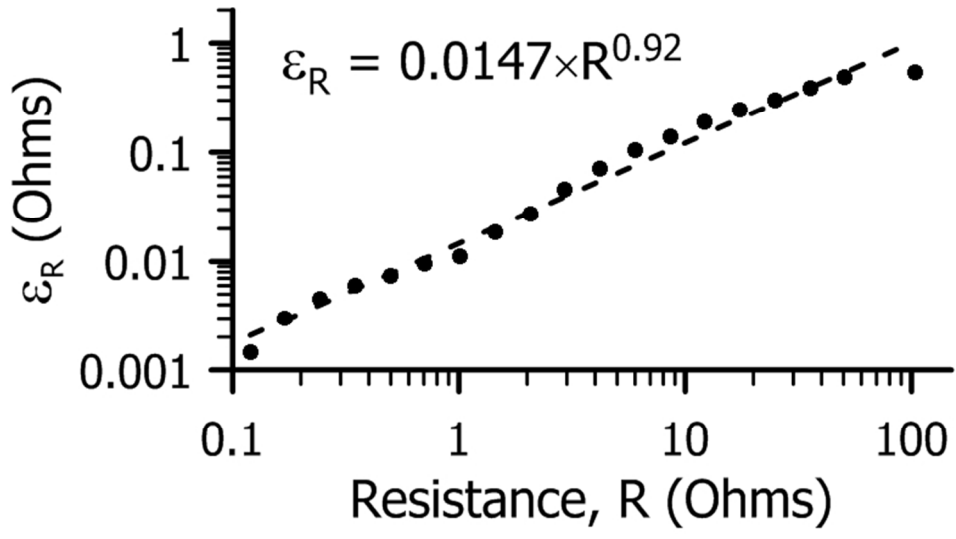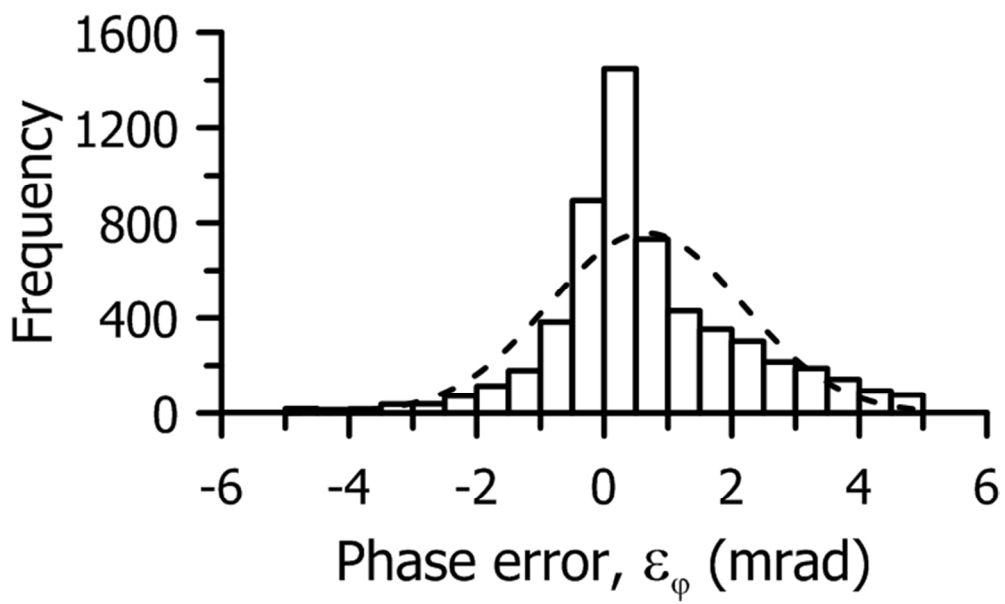886   Water Resources Research, 27(4): 533-546.

887

1
2
3
4
5
6
7
8
9
10
11
12
13
14
15
16
17
18
19
20
21
22
23
24
25
26
27
28
29
30
31
32
33
34
35
36
37
38
39
40
41
42
43
44
45
46
47
48
49
50
51
52
53
54
55
56
57
58
59
60

888   LIST OF FIGURES

889

908   Figure 11. Results of five-cluster analysis showing (a) clusters based on real conductivity and

909   (b) clusters based on real and imaginary conductivity.

910   Figure 12. Cluster analysis results for well C4: (a) real conductivity profile from inversion; (b)

911   imaginary conductivity profile from inversion; (c) cluster boundaries from five-cluster analysis;

912   (d) cluster boundaries from six-cluster analysis; (e) unit boundaries (Barrash and Clemo, 2002;

913   Mwenifumbo et al, 2009).

914   Figure 13. Cluster analysis results for well B4: (a) real conductivity profile from inversion; (b)

915   imaginary conductivity profile from inversion; (c) cluster boundaries from five-cluster analysis;

916   (d) cluster boundaries from six-cluster analysis; (e) unit boundaries (Barrash and Clemo, 2002;

917   Mwenifumbo et al, 2009).

918   Figure 14. Example profiles of hydraulic conductivity. Black line - values computed using

919   equation 7 using complex conductivity values. Grey line - values from multi-level slug test data

920   in Barrash and Cardiff (2013). Note closer correspondence in the lower portion of the

921   stratigraphy where K and porosity are more related in the Kozeny-Carman sense (Barrash and

922   Cardiff, 2013).
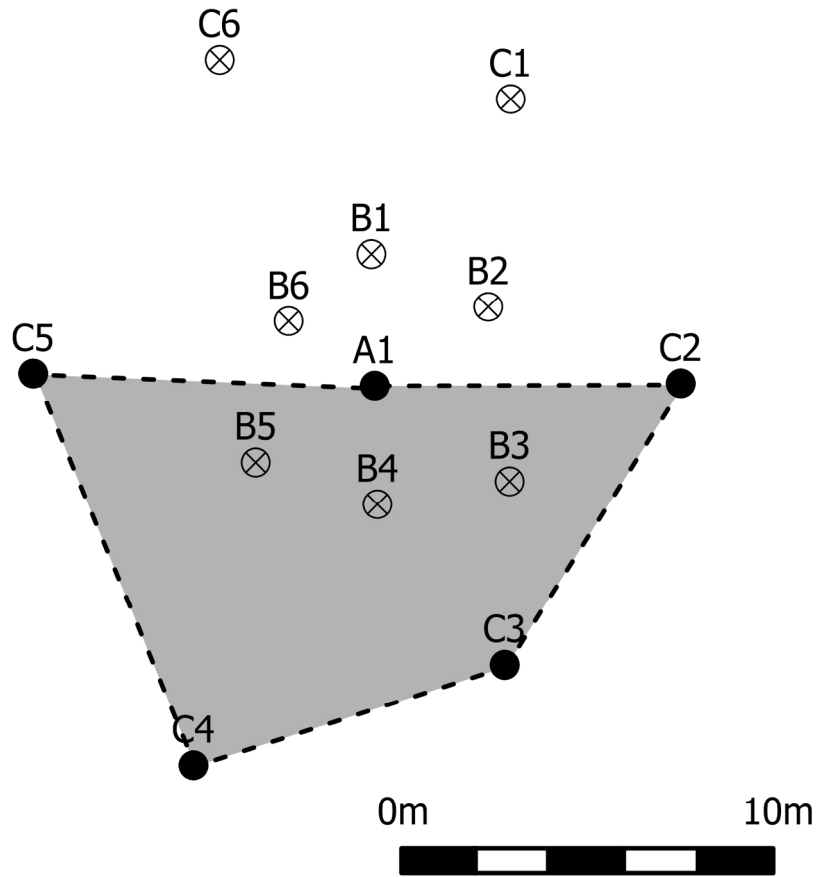
Layout of central wellfield at the BHRS. Solid symbols show location of electrode arrays. Shaded zone indicates area of investigation in this study.
169x170mm (300 x 300 DPI)
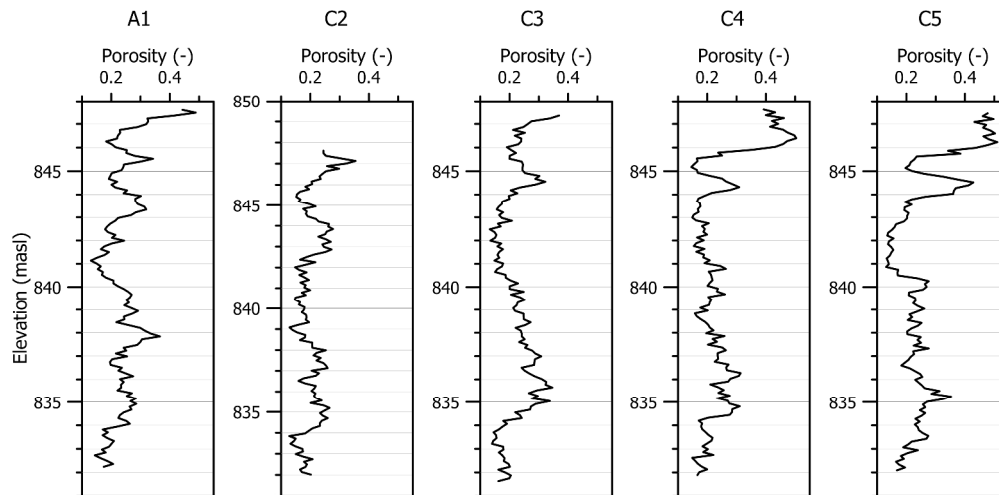
Example porosity profiles from central wellfield borehole logs.
379x186mm (300 x 300 DPI)
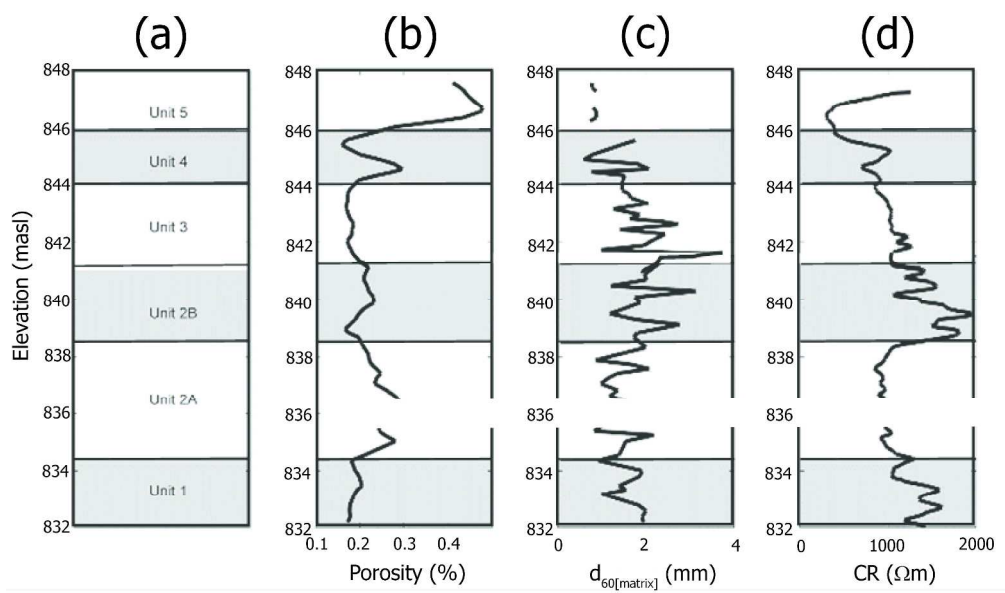
Profiles at borehole C4; (a) unit boundaries; (b) porosity; (c) d60 for the matrix only (d60[matrix]); (d) capacitive probe resistivity. Sources: Barrash and Clemo (2002); Reboulet and Barrash (2003); Mwenifumbo et al. (2009); Barrash and Cardiff (2013).
301x175mm (300 x 300 DPI)
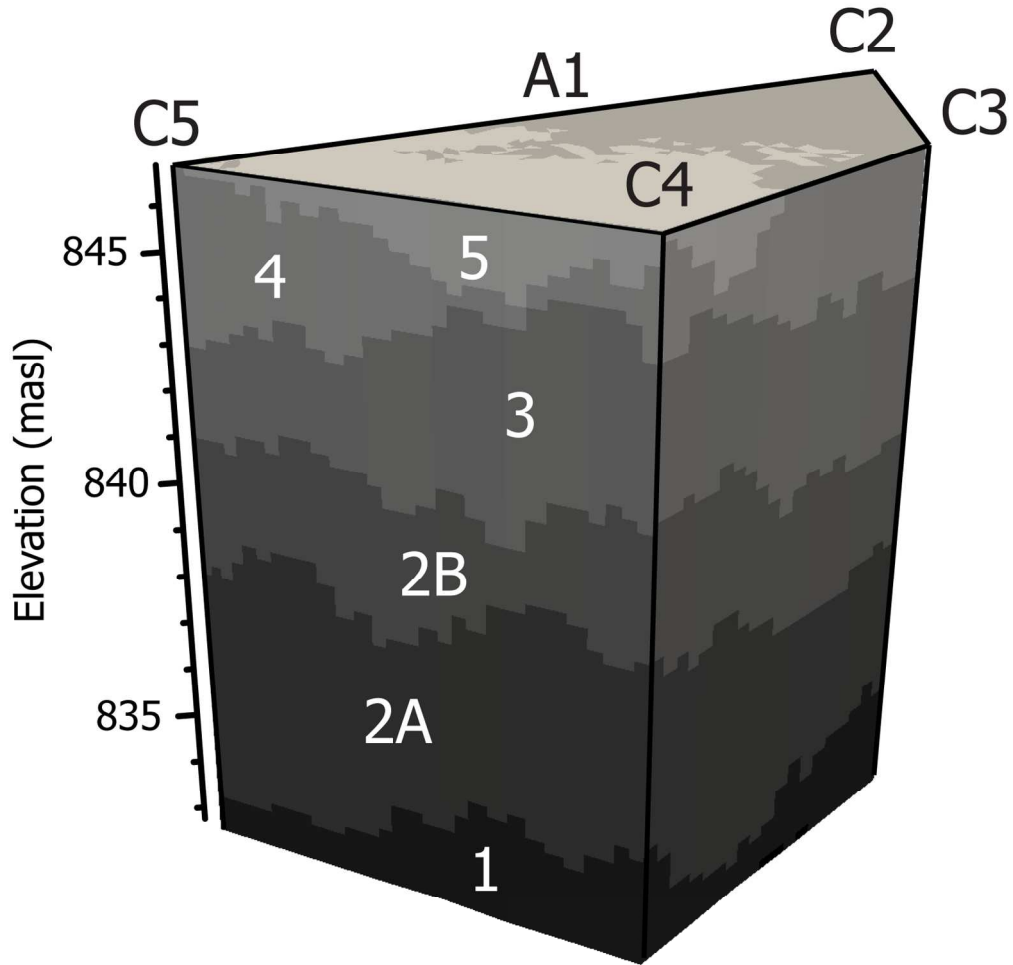
Example unit boundary realization based on a geostatistical model of unit contacts.
210x223mm (200 x 200 DPI)
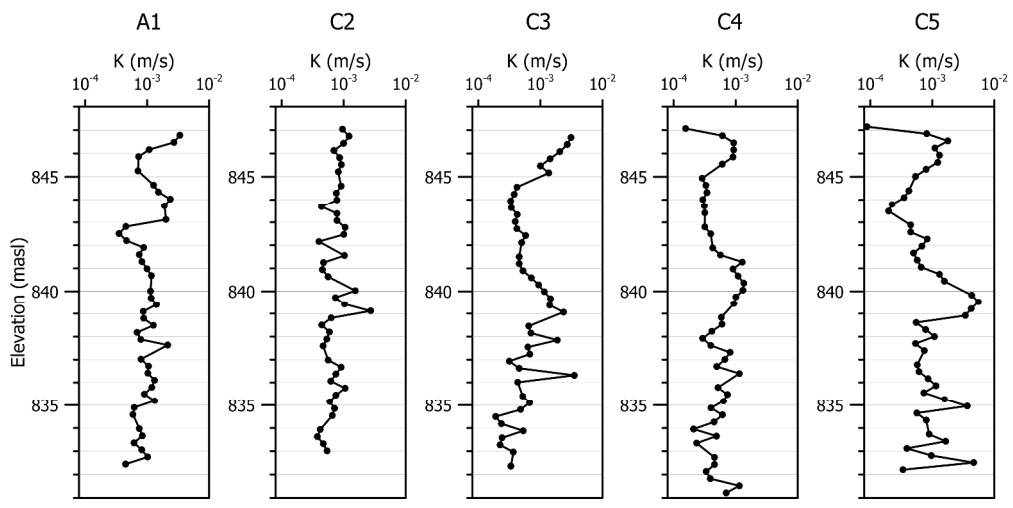
Example hydraulic conductivity profiles derived from multi-level slug tests [based on data in Barrash and Cardiff (2013)]
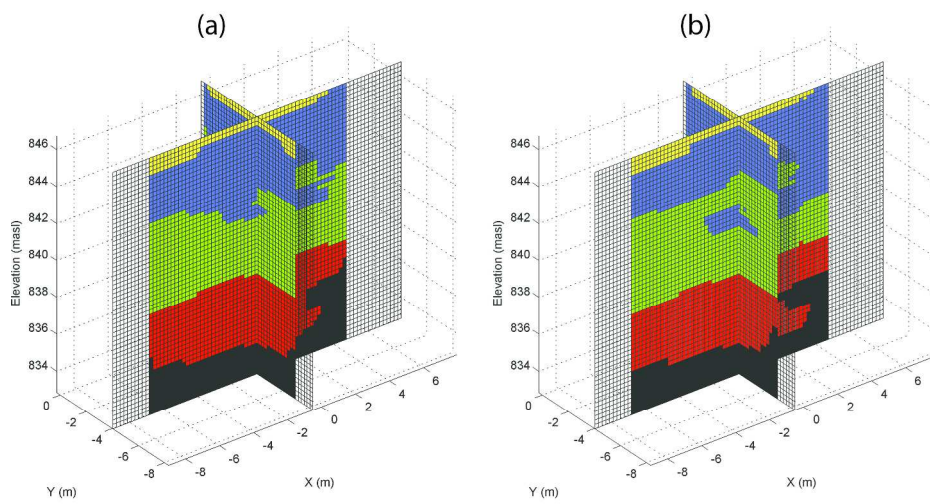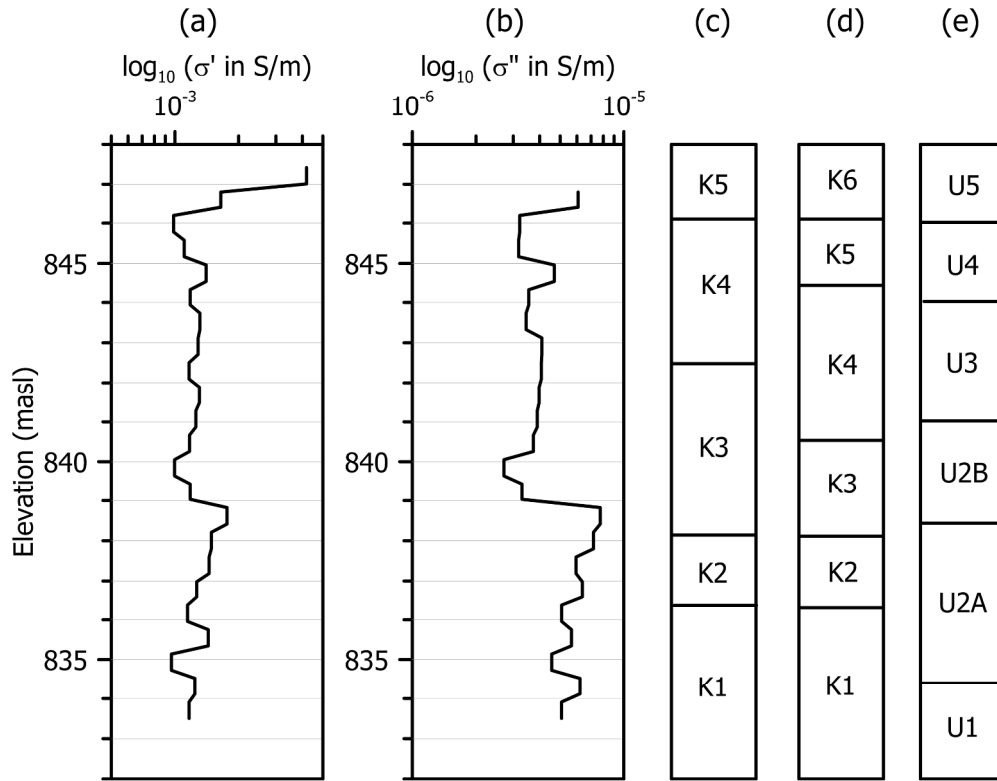384x188mm (300 x 300 DPI)

1
2
3
4
5
6
7
8
9
10
11
12
13
14
15
16
17
18
19
20
21
22
23
24
25
26
27
28
29
30
31
32
33
34
35
36
37
38
39
40
41
42
43
44
45
46
47
48
49
50
51
52
53
54
55
56
57
58
59
60

$$\varepsilon_R = 0.0147 \times R^{0.92}$$

$$\varepsilon_\varphi = 1.637 - 0.291 \times \ln(R)$$

Error relationships for complex resistivity data.
139x160mm (150 x 150 DPI)

Distribution of phase angle reciprocity errors. Dashed line shows Gaussian distribution for same sample mean and standard deviation as observed distribution.
130x81mm (150 x 150 DPI)
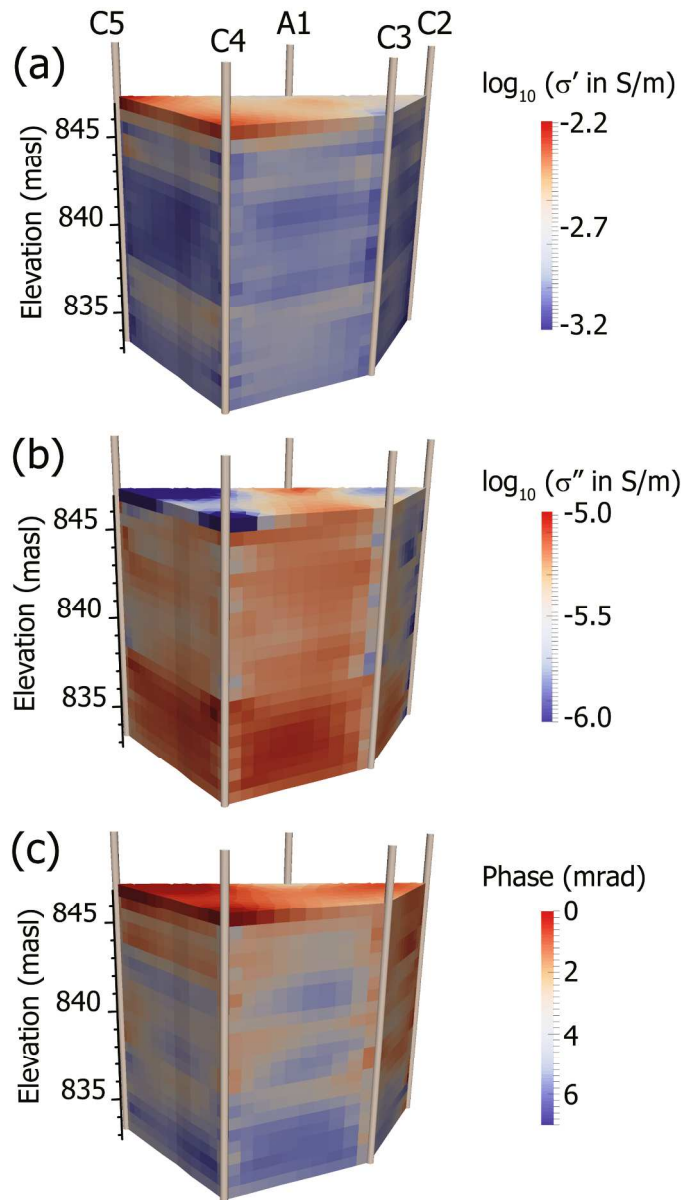
Complex resistivity inversion. (a) real conductivity; (b) imaginary conductivity; (c) phase angle.
137x245mm (300 x 300 DPI)

1
2
3
4
5
6
7
8
9
10
11
12
13
14
15
16
17
18
19
20
21
22
23
24
25
26
27
28
29
30
31
32
33
34
35
36
37
38
39
40
41
42
43
44
45
46
47
48
49
50
51
52
53
54
55
56
57
58
59
60
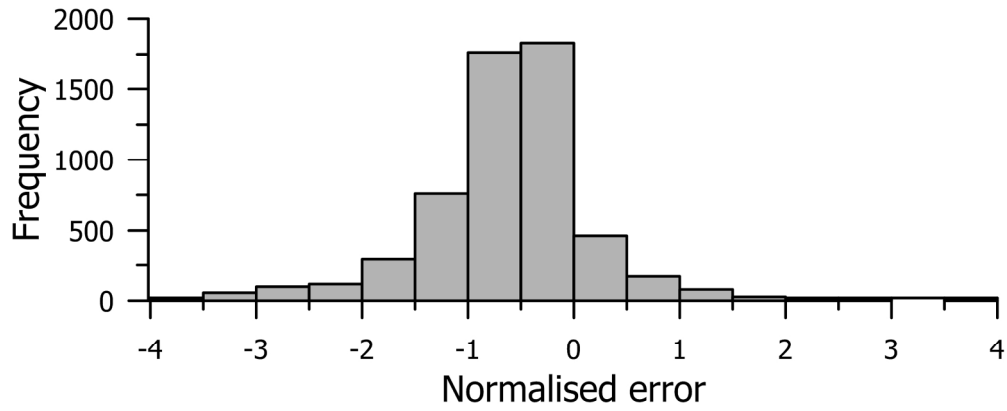
Distribution of normalized phase misfit for all measurements.
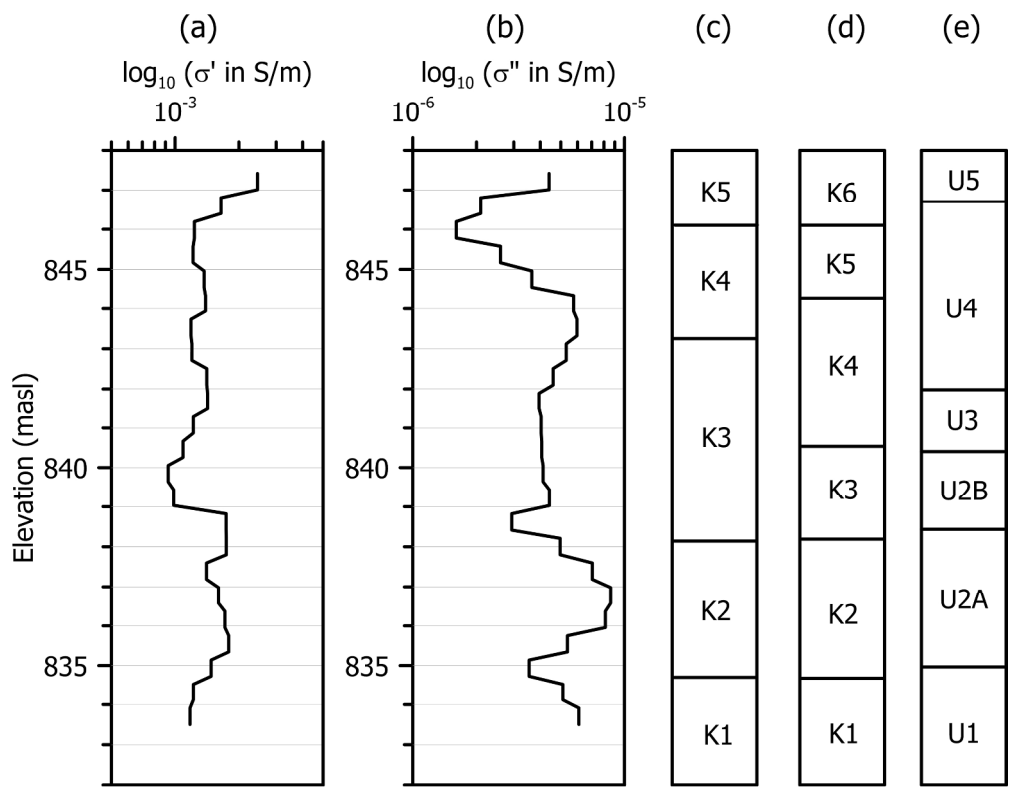177x81mm (300 x 300 DPI)

1
2
3
4
5
6
7
8
9
10
11
12
13
14
15
16
17
18
19
20
21
22
23
24
25
26
27
28
29
30
31
32
33
34
35
36
37
38
39
40
41
42
43
44
45
46
47
48
49
50
51
52
53
54
55
56
57
58
59
60
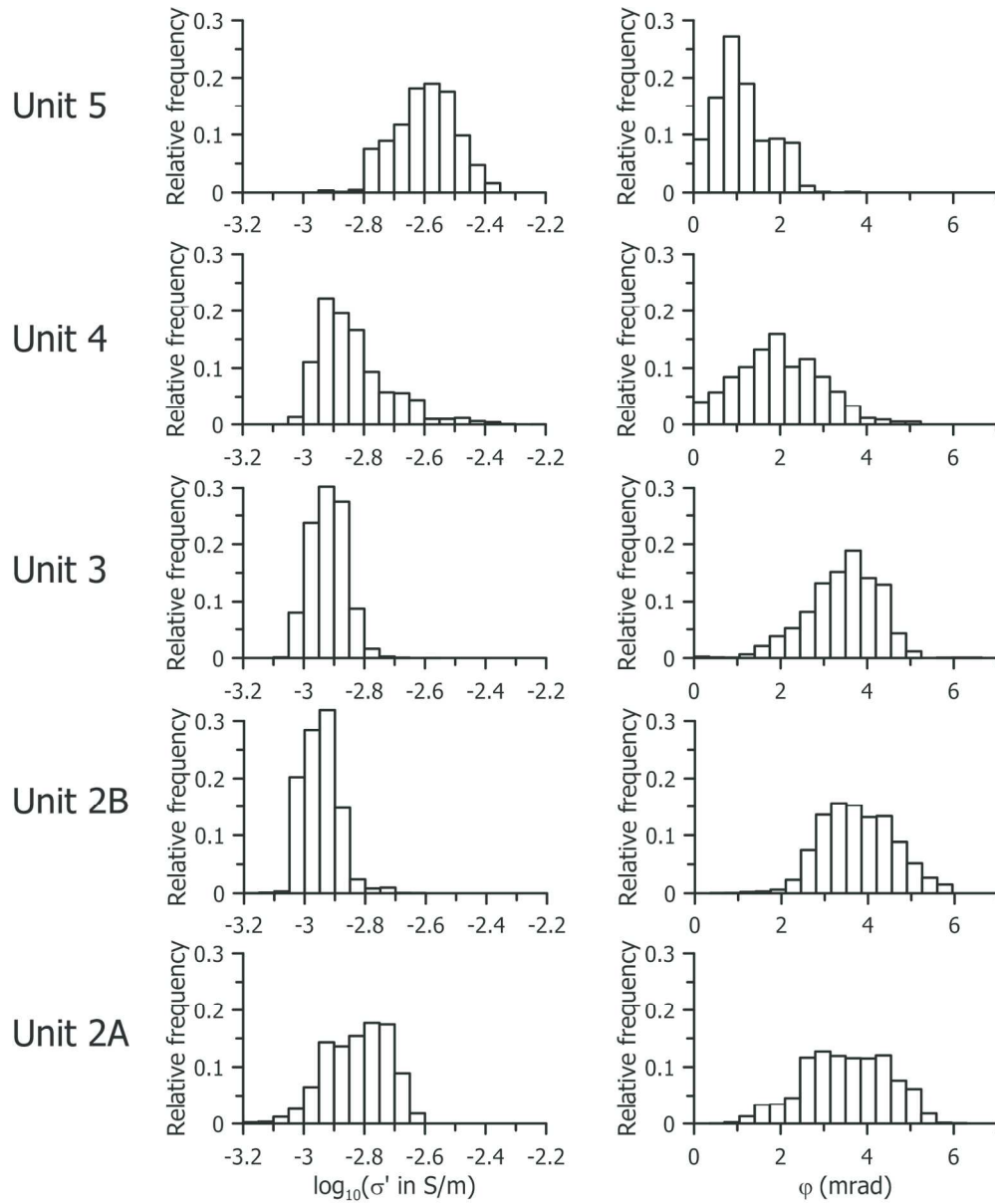
Variation in real conductivity magnitude (left column) and phase angle (right column) for image values in
Figure 8, delineated into units following the stratigraphy in Figure 4.
173x209mm (300 x 300 DPI)

Results of five-cluster analysis showing (a) clusters based on real conductivity and (b) clusters based on real and imaginary conductivity.
293x152mm (300 x 300 DPI)

Cluster analysis results for well C4: (a) real conductivity profile from inversion; (b) imaginary conductivity profile from inversion; (c) cluster boundaries from five-cluster analysis; (d) cluster boundaries from six-cluster analysis; (e) unit boundaries (Barrash and Clemo, 2002; Mwenifumbo et al, 2009).
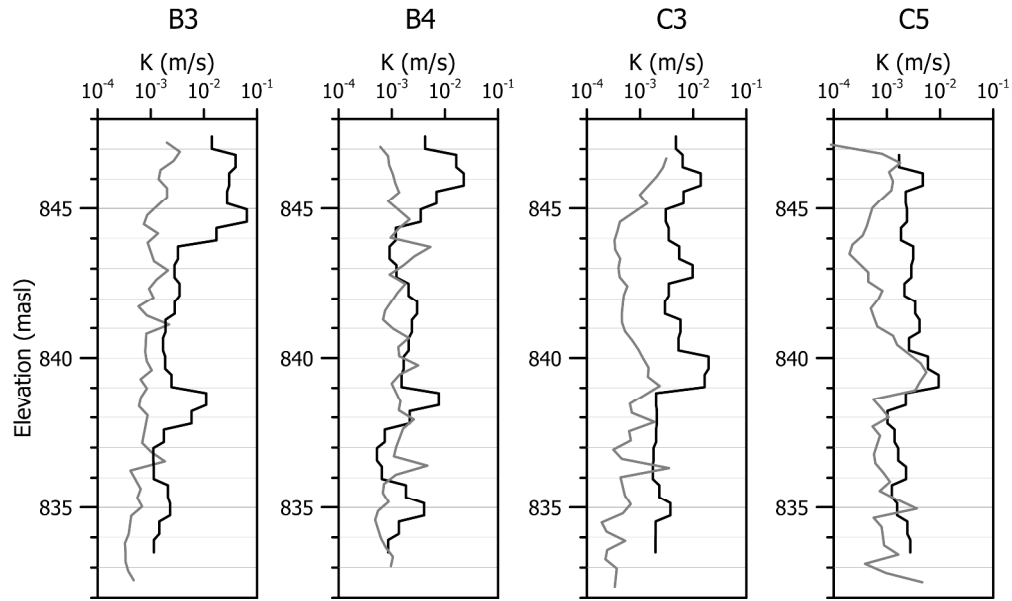236x184mm (300 x 300 DPI)

1
2
3
4
5
6
7
8
9
10
11
12
13
14
15
16
17
18
19
20
21
22
23
24
25
26
27
28
29
30
31
32
33
34
35
36
37
38
39
40
41
42
43
44
45
46
47
48
49
50
51
52
53
54
55
56
57
58
59
60

Cluster analysis results for well B4: (a) real conductivity profile from inversion; (b) imaginary conductivity profile from inversion; (c) cluster boundaries from five-cluster analysis; (d) cluster boundaries from six-cluster analysis; (e) unit boundaries (Barrash and Clemo, 2002; Mwenifumbo et al, 2009).
236x184mm (300 x 300 DPI)

Example profiles of hydraulic conductivity. Black line - values computed using equation 7 using complex conductivity values. Grey line - values from multi-level slug test data in Barrash and Cardiff (2013). Note closer correspondence in the lower portion of the stratigraphy where K and porosity are more related in the Kozeny-Carman sense (Barrash and Cardiff, 2013).

313x187mm (300 x 300 DPI)